Accepted Manuscript

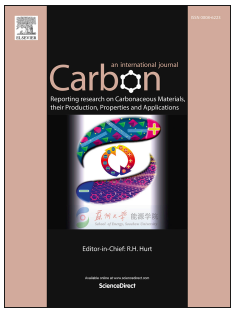

Quantitative atomic-scale structure characterization of ordered mesoporous carbon materials by solid state NMR

Zhuoran Wang, Naftali Opembe, Takeshi Kobayashi, Nicholas C. Nelson, Igor I. Slowing, Marek Pruski

PII: S0008-6223(18)30096-4

DOI: 10.1016/j.carbon.2018.01.087

Reference: CARBON 12828

To appear in: *Carbon*

Received Date: 23 December 2017

Revised Date: 22 January 2018

Accepted Date: 24 January 2018

Please cite this article as: Z. Wang, N. Opembe, T. Kobayashi, N.C. Nelson, I.I. Slowing, M. Pruski, Quantitative atomic-scale structure characterization of ordered mesoporous carbon materials by solid state NMR, *Carbon* (2018), doi: 10.1016/j.carbon.2018.01.087.

This is a PDF file of an unedited manuscript that has been accepted for publication. As a service to our customers we are providing this early version of the manuscript. The manuscript will undergo copyediting, typesetting, and review of the resulting proof before it is published in its final form. Please note that during the production process errors may be discovered which could affect the content, and all legal disclaimers that apply to the journal pertain.

templated by

Pluronic F127

Pyrolysis

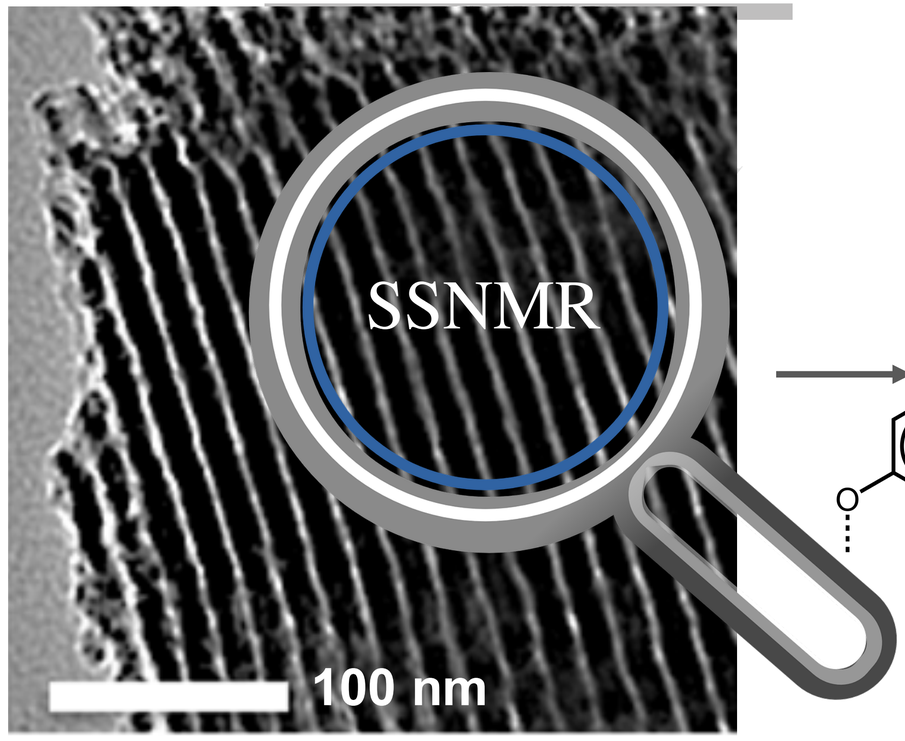

Ordered Mesoporous Carbon (OMC)

ACCEPTED MANUSCRIPT

Quantitative Atomic-Scale Structure Characterization of Ordered Mesoporous Carbon Materials by Solid State NMR

Zhuoran Wang,[a,b] *Naftali Opembe,*[b] *Takeshi Kobayashi,*[b] *Nicholas C. Nelson,*[a,b] *Igor I. Slowing*[*,a,b] *and Marek Pruski*[*,a,b]

[a] Department of Chemistry and [b] U.S. Department of Energy Ames Laboratory, Iowa State University, Ames, Iowa 50011, United States

ABSTRACT

Solid-state (SS)NMR techniques were applied to characterize the atomic-scale structures of ordered mesoporous carbon (OMC) materials prepared using Pluronic F127 as template with resorcinol and formaldehyde as polymerizing precursors. A rigorous quantitative analysis was developed using a combination of ^{13}C SSNMR spectra acquired with direct polarization and cross polarization on natural abundant and selectively ^{13}C-enriched series of samples pyrolyzed at various temperatures. These experiments identified and counted the key functional groups present in the OMCs at various stages of preparation and thermal treatment. The chemical evolution of molecular networks, the average sizes of aromatic clusters and the extended molecular structures of OMCs were then inferred by coupling this information with the elemental analysis results.

*Corresponding authors. Tel: 515 294-2017. E-mail: mpruski@iastate.edu (Marek Pruski).
Tel: 515 1959. E-mail: islowing@iastate.edu (Igor I. Slowing).

ACCEPTED MANUSCRIPT

1. INTRODUCTION

Since their discovery almost two decades ago[1, 2], ordered mesoporous carbon (OMC) materials have drawn great interest due to the robustness, chemical inertness, low density and high accessibility of their frameworks[2-6]. Potential applications of OMCs in drug delivery[7, 8], energy storage[9], sensors[10], separations[11], and catalysis[12] have motivated studies of their structures and properties, as well as efforts toward the development of increasingly efficient manufacturing methods.

Commonly employed characterization techniques for OMCs include X-ray diffraction (XRD), small-angle X-ray scattering (SAXS), thermogravimetric analysis (TGA), transmission electron microscopy (TEM), scanning electron microscopy (SEM), and nitrogen physisorption[6, 13-16]. The resulting information relates to important structural properties of OMCs on the mesoscopic and microscopic levels, such as spatial arrangement of mesopores, unit cell parameters, specific surface area, and pore width distribution.

The chemical properties and performance of these materials, however, are governed by their atomic-scale structure, which has been much less studied. Notable efforts included works by Zhao et al. and Dai et al., who monitored the structural evolution of the OMC materials, derived from phenol-formaldehyde resins and triblock copolymer templates, during the synthesis and pyrolysis using elemental analysis, TGA, Fourier transform infrared spectroscopy (FTIR), and ^{13}C solid-state NMR (SSNMR)[15, 17, 18]. These studies identified the key functional groups present in OMCs at various stages of preparation and thermal treatment; however, they did not include precise identification of the molecular structures or the underlying reaction mechanisms. Kim et al.[19] and Jiang et al.[20] on the other hand, studied the structural evolution of non-templated phenol-formaldehyde resins upon pyrolysis. The pyrolysis mechanisms and the resulting polycyclic aromatic structures were deduced based on combinations of FTIR[19, 20], TGA[19], elemental analysis[19], and gas chromatography mass spectroscopy (GC-MS)[20].

Here, we set out to refine the understanding of the structural evolution of OMC materials through rigorous quantitative SSNMR analysis of their atomic-scale structures following pyrolysis at temperatures between 300˚C and 900˚C. The materials were prepared using Pluronic F127 as a template and resorcinol and formaldehyde as precursors, and their mesoscale structural properties were determined by XRD, TEM and nitrogen sorption methods. The ^{13}C chemical shift information was obtained from the SSNMR spectra measured on samples prepared with natural abundance and ^{13}C-enriched formaldehyde. To determine the distribution of carbon functionalities in OMCs we used a modified SSNMR approach inspired by the previous studies on coals[21, 22]. The evolution of the extended molecular structures of OMCs pyrolyzed at various temperatures was then inferred by coupling this information with the elemental analysis results.

2. EXPERIMENTAL SECTION

Reagents. Deionized water (18 MΩ·cm resistivity) was generated in-house using a Barnstead e-pure purification system. Formaldehyde, ^{13}C-labeled formaldehyde (99% ^{13}C), Pluronic F127, resorcinol (>99% pure), cyclohexane (>99% pure), and hydrochloric acid (concentrated) were purchased from Sigma Aldrich. Ethanol (absolute, 200 proof) was purchased from Decon Laboratories. All reagents were used as received without further purification.

Synthesis of OMCs. The samples were synthesized following the previously published method[18]. Pluronic F127 was used as template with resorcinol and formaldehyde as polymerizing precursors in acidified ethanol. Typically, absolute ethanol (4.5 mL) and HCl (3.0 M, 4.5 mL) were mixed, followed by sequential addition of Pluronic F127 (1.1 g), resorcinol (1.1 g, 10 mmol), and formaldehyde (1.3 g, 16 mmol). The mixture was stirred at room temperature for ca. 40 min and then transferred to a 15 mL centrifuge tube to separate the aqueous layer from a thick gel at 10000 rpm for 15 min. The gel was cast onto a petri-dish and dried at room temperature overnight. The resultant product was subsequently cured at 80 ˚C and subsequently at 120 ˚C for 24 h each.

The same procedure was used to prepare the ^{13}C-enriched samples, except for using ^{13}C-labeled formaldehyde. The amounts of all components were adjusted to maintain the overall resorcinol/F127/formaldehyde weight ratio as in the original synthesis.

All cured samples were pyrolyzed under N_2 flow for 6 h at either 300 °C, 400°C, 500 °C, or 900 °C, with ramp rate of 1 °C·min^{-1}. The natural abundance and ^{13}C-enriched samples are denoted as OMCx and OMCx$_{13C}$, respectively, where x is the pyrolysis temperature.

XRD. Low angle X-ray diffraction patterns were obtained using a Bruker AXS D8 Discover powder diffractometer at 40 kV, 40 mA for CuKα (λ = 1.5406 Å) in a continuous PSD fast mode using a Linxeye Xe (full open) detector. Data were acquired with 1°/s steps. No spinning was applied to the samples and the diffracted divergence slit was left open. Data were analyzed using the DIFFRAC.EVA program from the Bruker Powder Analysis Software package.

Nitrogen Sorption Isotherms. Nitrogen sorption isotherms were measured on a Micrometrics Tristar 3000 surface area and porosity analyzer at liquid nitrogen temperature (-196 ˚C). Before analysis, the samples were degassed at 100 ˚C for 6 hours under the flow of N_2 (100 sccm). The specific surface areas were calculated using the Brunauer-Emmett-Teller (BET) method[23] and the pore size distribution plots were derived based on the Barret-Joyner-Halenda (BJH) model[24].

Elemental Analysis. Elemental analyses were performed on a Perkin Elmer 2100 Series II CNH/S (carbon, nitrogen, hydrogen and sulfur) analyzer, with acetanilide as an internal standard. Combustion and reduction temperatures were set at 925 ˚C and 640 ˚C, respectively. Prior to analysis samples were dried at 100 °C under vacuum for 12 h and then kept under vacuum at room temperature. Because the synthesis did not involve any sources of sulfur and nitrogen, the instrument was not configured to quantify sulfur. The nitrogen content was measured by default in the standard configuration, however, all samples yielded negligibly small values of ≤ 0.12 wt%. The weight percentages of oxygen were calculated from the difference between the total mass and the mass of carbon and hydrogen. All samples

were analyzed in triplicate, and the reported results are the average values. The instrument accuracy specification is ±0.3% based upon a triplicate analysis.

Electron Microscopy. Transmission electron microscopy images were taken using a FEI Tecnai G2 F20 field emission microscope operating at 200 kV (point-to-point resolution <0.25 nm and a line-to-line resolution of <0.10 nm). Samples were prepared by placing 2−3 drops of dilute ethanol suspensions onto lacey carbon-coated copper grids.

Solid-State NMR. The ^{13}C NMR spectra were obtained on a Varian NMR System 600 MHz (14.1 T) spectrometer equipped with a Varian 1.6-mm probe capable of magic angle spinning (MAS) at 40 kHz and an Agilent DD2 400 MHz (9.4 T) spectrometer equipped with a 5-mm Chemagnetics probe operated under MAS at 10 kHz. The experiments included direct-polarization MAS and ^{1}H→^{13}C cross-polarization MAS, herein denoted as ^{13}C DPMAS and ^{13}C CPMAS, respectively. To eliminate the considerable carbon background present in the DPMAS-based experiments, all of the Teflon components of the 5-mm MAS rotors were replaced with parts custom-made for the present study of boron nitride. The background signals originating from the probes' static components were dephased by the spin-echo sequence used in our measurements (see below).

The experimental parameters are given in the figure captions using the following notation: ν_R denotes the MAS rate, τ_R is the rotor period ($\tau_R = \nu_R^{-1}$), τ_{CP} is the contact time during CP, $\nu_{RF}(^{1}H)$ and $\nu_{RF}(^{13}C)$ are the magnitudes of RF magnetic fields at ^{1}H and ^{13}C frequencies, τ_{RD} is the recycle delay, NS is the number of scans, and AT is the total acquisition time. The ^{13}C NMR chemical shifts are externally referenced to TMS at δ_{13C} = 0 ppm, using 4,4-dimentyl-4-silapentane-1-sulfonic acid as a secondary reference.

3. RESULTS AND DISCUSSION

The paper is organized as follows. In the section below we report the nano- and mesoscale structural properties of prepared OMCs derived from TEM, XRD and nitrogen sorption analysis. A discussion of

^{13}C SSNMR spectra is then presented, and followed with the description of our approach for estimating the relative concentrations of carbon functionalities. In the last two sections, we discuss the evolution of extended molecular networks in OMC300, OMC400 and OMC500 materials and propose their average molecular structures.

Textural Characterization. The mesoporous character of OMCs is evidenced by the type IV N_2 sorption isotherms with sharp condensation steps at P/P_0 of 0.5 to 0.6 (Figure S1a in SI). The ordered structure of these mesopores is demonstrated in the corresponding TEM images (Figure 1**)** and XRD patterns (Figure S1c in SI). The specific surface areas (S_{BET}), total pore volumes (V_{BJH}), pore widths (w_{BJH}), spacings between the pores (d(100)) derived from the XRD patterns, wall thicknesses, and elemental analyses data for all OMC materials are summarized in Table 1. Whereas increasing the carbonization temperature has led to larger surface areas and pore volumes, it also shifted the mesopore width distributions to lower values (Table 1 and Figure S1b in SI). Estimation of the unit cell parameters from the sharp reflections at $2\theta < 1°$ indicates shrinking of the mesoporous framework with pyrolysis temperature[25], and is consistent with the pore width contraction. In addition to the intense reflection corresponding to the (100) plane of the 2D hexagonal pore array, OMC300 and OMC400 display two higher order reflections assigned to the (110) and (200) planes confirming the *p6mm* symmetry of the mesopores[15, 25]. These reflections are hardly observed in OMC500 and absent in OMC900, suggesting that increasing carbonization temperatures are detrimental to the mesostructure of the materials. The observed reorganization of the mesoscale order, framework shrinking, and increased formation of micropores is caused by changes in the molecular structure of the materials induced by pyrolysis, and evolution of gaseous byproducts including H_2, H_2O, and CO_2[18] as discussed below.

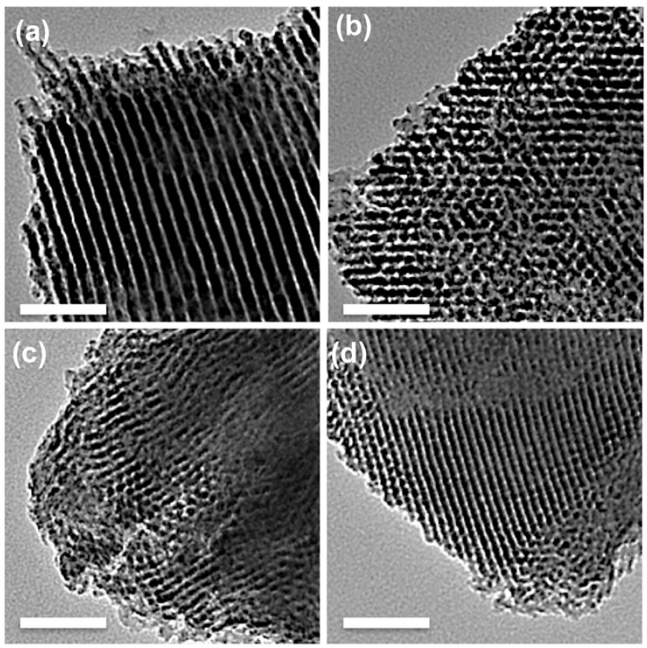

Figure 1. TEM images of (a) OMC300, (b) OMC400, (c) OMC500 and (d) OMC900. Scale bar is 100 nm for all images. Images represent regions of samples that were exposed to no or minimal beam damage.

Table 1. Structural properties of OMC materials carbonized at different temperatures.

Sample	S_{BET} ($m^2 \cdot g^{-1}$)	V_{BJH} ($cm^3 \cdot g^{-1}$)	w_{BJH} (Å)	d(100) (Å)	Wall Thickness[a] (Å)	Elemental analysis (at.%)		
						C	H	O
OMC300	570	0.597	65	137	93	44.9	44.9	10.2
OMC400	599	0.587	65	131	86	57.1	34.3	8.6
OMC500	700	0.611	55	125	89	62.0	33.8	4.2
OMC900	1055	0.717	55	110	72	88.5	10.8	0.7

[a] Wall thickness obtained by subtracting w_{BJH} from a_o where $a_o = 2 \times d(100)/\sqrt{3}$[26].

SSNMR: ^{13}C DPMAS and CPMAS Spectra. The ^{13}C DPMAS and ^{13}C CPMAS spectra of natural abundance and ^{13}C-enriched OMCs, acquired at 14.1 T using a 1.6-mm MAS probe, are shown in Figures 2 (DPMAS) and S2 in SI (CPMAS). It is well known that the CPMAS method, while fast and efficient, has a drawback, in that the polarization efficiency is strongly dependent on the ^{1}H-^{13}C internuclear distances and molecular motions, thereby inhibiting quantitative detection of all ^{13}C nuclei

[27]. In the case of OMCs, uniform excitation of carbons by CP can be particularly difficult to achieve because of the low hydrogen content and the influence of paramagnetic interaction, which accelerates the so-called $T_{1\rho}$ relaxation[27]. The DPMAS experiment, on the other hand, can result in uniform excitation of all ^{13}C nuclei and thus yield a quantitative spectrum, but requires a long recycle delay to allow for full recovery of thermal equilibrium of ^{13}C spins. These features are on display in Figures 2 and S2. Indeed, the CPMAS measurements were 10-30 times faster and yielded better signal-to-noise ratio than DPMAS, which required long recycle delays of 30-45 s to assure quantitative accuracy of the spectra. However, in spite of using a long CP contact time (τ_{CP} = 1.5 ms), the CPMAS method discriminated against non-protonated carbons in the larger clusters of aromatic rings. Thus, we will use both sets of spectra for peak assignment, structural analysis and relaxation measurements, but rely on DPMAS for accurate relative peak intensities (*vide infra*).

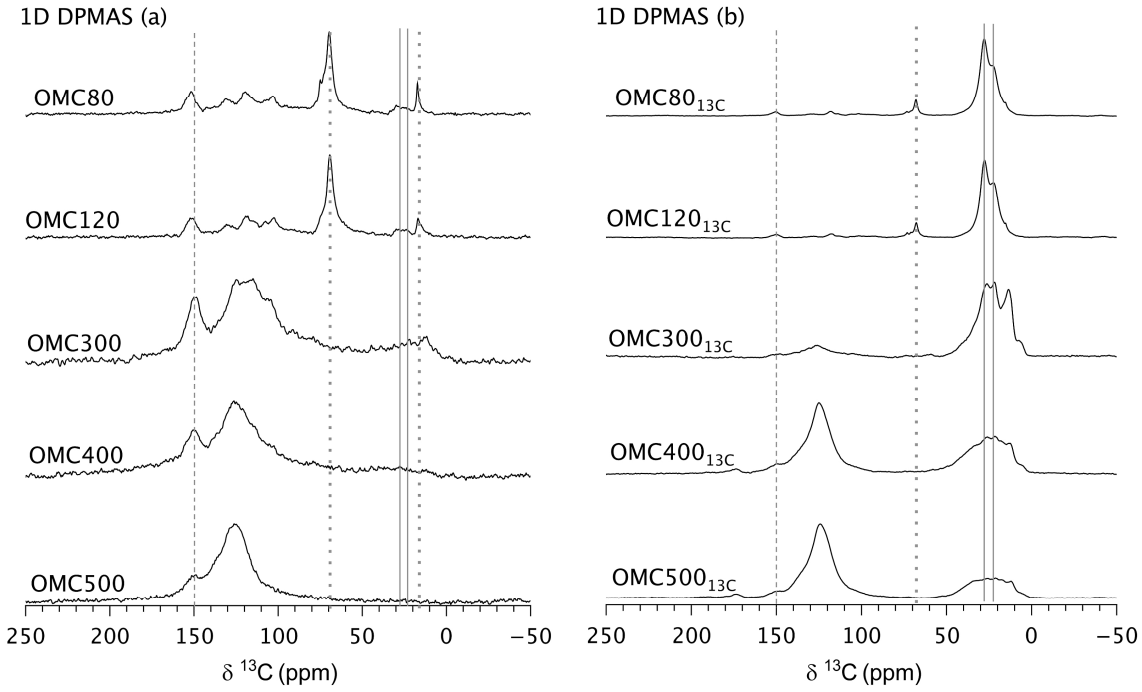

Figure 2. The ^{13}C DPMAS spectra of OMC (a) and OMC$_{13C}$ (b) materials. The spectra were normalized to highest peak. The spectra were acquired at 14.1 T using ν_R = 40 kHz, $\nu_{RF}(^{13}C)$ = 100 kHz, $\nu_{RF}(^{1}H)$ = 10 kHz during TPPM decoupling, τ_{RD} = 30 s (a), τ_{RD} = 45 s (b), NS = 2000 (a) and NS = 1800 (b).

The DPMAS spectra of non-carbonized materials prepared from naturally-abundant formaldehyde (OMC80 and OMC120 in Figure 2a) feature resonances at δ_{13C} = 70 and 16 ppm, marked with dotted lines, representing the methylene and methyl groups in the residual molecules of the template (Pluronic F127) remaining inside the pores[28, 29]. These resonances are partly suppressed in the corresponding CPMAS spectra (Figure S2a in SI) due to motions of template molecules in the kHz range. Also present in these spectra are resonances assignable to low-temperature products of resorcinol-formaldehyde polymerization, including a peak at $\delta_{13C} \approx$ 150 ppm due to phenolic carbon (dashed line), several peaks in the 110-140 ppm region representing aromatic carbons C2, C4, C5 and C6 shown in Figure 3, and resonances at $\delta_{13C} \approx$ 24 and 28 ppm discussed in the paragraph below[30]. Chemical shift information for resorcinol and formaldehyde are included in the supplemental information (S7).

The DPMAS and CPMAS measurements on the equivalent ^{13}C-enriched samples ($OMC80_{13C}$ and $OMC120_{13C}$) selectively highlighted carbon linkages between the aromatic rings, as the isotope enrichment was applied exclusively to formaldehyde. The resulting spectra are dominated by partly resolved peaks centered at $\delta_{13C} \approx$ 24 and 28 ppm (solid lines), assigned to Ar–CH_2–Ar links between the resorcinol aromatic rings. The more intense resonance at 28 ppm corresponds to linkages connecting carbons C4-C4, C4-C6, and C6-C6, whereas the position of the weaker peak matches well with the chemical shift of 24 ppm expected for C2-C4(6) pairs (note that C4 and C6 are equivalent)[30]. We did not observe a peak near 18 ppm expected for C2–CH_2–C2 links[30], or the resonances expected for single C5–CH_2–C4(6) and C5–CH_2–C5 links, expected at $\delta_{13C} \approx$ 36 ppm and 40 ppm[31], respectively. We did not find literature data for the chemical shift corresponding to C5–CH_2–C2, although such link is less likely to form due to the low reactivity of C5. However, our spectra do support the presence of two –CH_2– links between adjacent resorcinol aromatic rings. Based on the ^{13}C chemical shifts predicted by ChemDraw, a methylene resonance in the C5–CH_2–C4 link adjacent to a corresponding C4–CH_2–C5 link, such as one depicted in Figure 7 below, is expected precisely at $\delta_{13C} \approx$ 28 ppm. Importantly, the spectra of $OMC80_{13C}$ and $OMC120_{13C}$ demonstrate that few, if any, links involve the O atoms in

resorcinol and that most of the O atoms in formaldehyde are eliminated prior to pyrolysis. In particular, this synthesis did not yield structures like C_{Ar}–O–CH_2–C_{Ar} (expected at $\delta_{13C} \approx 70$ ppm[32]), C_{Ar}–O–CH_2–O–C_{Ar} ($\delta_{13C} \approx 90$ ppm[32]), or C_{Ar}–CH_2–O–… ($\delta_{13C} \approx 55$-75 ppm[30]), contrary to what has been proposed in ref [19]).

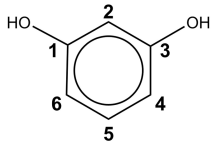

Figure 3. The carbon positions in resorcinol.

The structures of OMCs changed considerably as the result of pyrolysis. First, the DPMAS and CPMAS spectra of OMC300, OMC400 and OMC500 no longer show resonances attributable to Pluronic F127 (Figure 2 and S2). Second, the spectra of naturally ^{13}C-abundant samples (Figure 2a and S2a) present a broad resonance band at 110-140 ppm due to protonated and non-protonated aromatic carbons. The center of gravity of this band shifts downfield as the temperature of pyrolysis is increased, suggesting the advancement of polycyclization. The partly resolved peak at 150 ppm, which features prominently in the spectra of OMC80, OMC120 and OMC300, becomes comparatively weaker in OMC400 and OMC500, indicating loss of oxygen-bound aromatic carbons. The spectra of $OMC300_{13C}$, $OMC400_{13C}$ and $OMC500_{13C}$ (Figure 2b and S2b) show an increase in the aromatic peak intensity at the expense of the aliphatic carbons (see Table 2), which is also consistent with the progressing polycyclization[19, 20], and a peak centered at ~15 ppm, indicating the appearance of methyl groups. These observations suggest methylene disproportionation into aromatic and methyl carbons as the framework rearranges at the molecular level: 2 (–CH_2–) → =CH– + –CH_3 (*vide infra*).

We finally note that the sample pyrolyzed at 900 ˚C (OMC900) was not amenable to SSNMR investigation. To spin this sample under MAS, we had to dilute it with powdered sulfur in a 1:10 ratio, which implied that the sample is highly conductive[33]. Even then, however, we were unable to spin it

at above 6 kHz (in a 5-mm rotor) and could not elicit any measurable ^{13}C signal neither in DPMAS nor CPMAS experiments performed at 9.4 T. This failure can be attributed to a combination of several factors. First, the ~10-fold decrease in the number of observable nuclei due to dilution would necessitate the use of ~100 times longer data acquisitions to match the spectral quality of other samples. Second, the use of MAS at 6 kHz must have produced strong spinning sidebands, spaced by 60 ppm, which partly overlapped with the centerbands, as well as each other, further degrading sensitivity and resolution. Third, these sidebands could be additionally broadened by the magnetic susceptibility effects, often observed in carbon graphite-like materials heated at high temperatures[34]. Finally, the CPMAS intensity was additionally reduced due to low ^{1}H content (10.8 at%) in OMC900.

SSNMR: Quantitative Measurement of Carbon Functionalities. The chemical shift information alone is not sufficient to determine the extended atomic-scale structures of OMC materials. However, the *average* molecular structures of OMCs can be elucidated by combining spectral editing of quantitative SSNMR spectra with elemental analysis. To this end, we used SSNMR to quantitatively estimate the overall ratios of aliphatic (F_{al}) and aromatic (F_{ar}) carbons in the OMCs, as well as fractions of aromatic carbons that are protonated (f_{ar}^{H}) and nonprotonated (f_{ar}^{N})[22]. Note that our designation of f_{ar}^{N} does not include the oxygen-bound aromatic carbons in the OMCs, which are observed at around 150 ppm and can be quantified separately by deconvoluting the aromatic band in the spectra to determine the corresponding values of f_{ar}^{O}, such that $f_{ar}^{H} + f_{ar}^{N} + f_{ar}^{O} = 1$.

Determination of F_{al} and F_{ar}. The ratios of aliphatic (F_{al}) and aromatic (F_{ar}) carbons in the OMCs were estimated from the intensities of DPMAS spectra in Figure 2. For non-pyrolyzed samples, these ratios were obtained directly by integrating the top 2 spectra in Figure 2a (excluding Pluronic F127), yielding F_{al} = 0.17 (F_{ar} = 0.83) for OMC80, and F_{al} = 0.15 (F_{ar} = 0.85) for OMC120. For the sample pyrolyzed at 300 °C, we compared the results obtained from the integration of the DPMAS spectra of natural-abundance and ^{13}C-enrichd samples. In the case of $OMC300_{13C}$, we divided the intensity of the aliphatic peak by 90, to account for the 99% ^{13}C enrichment (note that natural ^{13}C abundance is 1.1%).

Both spectra yielded the same result (F_{al} = 0.09 and F_{ar} = 0.91), as expected given that ^{13}C enrichment did not significantly affect the aromatic intensity at this temperature. However, polycyclization did occur at temperatures above 300 ˚C, rendering the aliphatic intensity of OMC400 and OMC500 too low to be reliably estimated. Instead, we used the spectra of $OMC400_{13C}$ and $OMC500_{13C}$ to determine the fraction of ^{13}C nuclei that became aromatic due to ring condensation. By doing so, we were able to estimate the F_{al} vales for OMC400 and OMC500 at 0.04 and 0.03, respectively. These results are summarized in Table 2 below.

Determination of f_{ar}^{H}, f_{ar}^{N} and f_{ar}^{O}. In the case of disordered carbonaceous materials such as OMCs, an accurate measurement of f_{ar}^{H} and f_{ar}^{N} poses a considerable challenge. First, the highly sensitive CPMAS method does not provide quantitative ^{13}C intensities in these materials, as noted above. To further complicate matters, the protonated and nonprotonated aromatic carbon functionalities are unresolved in the OMC materials, being superimposed in the featureless broad band centered at around 130 ppm. Accordingly, a rigorous measurement of f_{ar}^{H} and f_{ar}^{N} values in OMCs requires the use of time-consuming, DPMAS-based spectral editing techniques. We tailored a customized approach to this measurement, which we now describe.

The most common technique for spectral editing of ^{13}C CPMAS spectra is referred to as dipolar C-H dephasing[35], and has been used extensively to differentiate non-protonated carbon functionalities at low magnetic fields (<9.4 T) under slow MAS. However, modern spectrometers operate at magnetic fields of at least 9.4 T, and thus require faster MAS to reduce the number and intensity of the spinning sidebands. Unfortunately, the dipolar dephasing method fails at MAS rates exceeding 5 kHz due to accelerated rotational recoupling of C-H dipolar interactions, which interferes with the dephasing process[36]. To circumvent this drawback, we proposed to take advantage of different responses of these carbons to MAS-synchronized spin-echo refocusing (T_2' relaxation)[36]. In this earlier study, the experiment was carried out under fast MAS (40 kHz), and exploited a simple spin-echo pulse sequence (Figure 4) to measure the intensities of various carbon resonances as a function of rotor-synchronized

interpulse delay $\tau = 2n\tau_R$. Similarly to dipolar dephasing, the time evolutions of carbon intensities during τ were governed by heteronuclear ^{1}H-^{13}C dipolar interactions, which were not completely averaged by MAS in the presence of strong homonuclear ^{1}H-^{1}H couplings, and were thus very different between protonated and nonprotonated carbons. With the overall time scale of these evolutions being extended from tens of μs (in the case of dipolar dephasing) to ms range, the spin-echo approach proved to be a reliable tool for spectral editing under fast MAS, allowing for quantitative estimates of f_{ar}^{H} and f_{ar}^{N} values, even in spectra which lacked resolution[36].

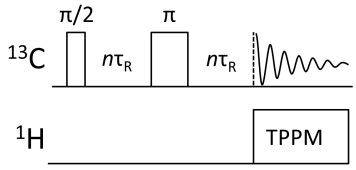

Figure 4. Pulse sequence used for acquiring spin-echo dephasing spectra. Experimental parameters: $\nu_{RF}(^{13}C)$ = 40 kHz, $\nu_{RF}(^{1}H$ TPPM) = 40 kHz, ν_R = 10 kHz, and τ_{RD} = 45 s. The experiment was repeated using 21 rotor-synchronized delays for $1 \le n \le 43$, each with NS = 160 (AT = ~ 43 h).

The shortcoming of this approach is, however, that a series of DPMAS spectra with different values of τ must be collected for each sample to reliably fit the spin-echo decay. In consideration of the fact that in OMCs such spectra must be acquired with a delay of 45 s, making each experiment very time-consuming with a fast MAS 1.6-mm rotor, we proposed to further modify the above strategy by using a 5-mm MAS probe by Chemagnetics with ~20 times larger rotor capacity. This can offer a substantial sensitivity advantage, provided that MAS at 10 kHz is sufficient to differentiate T_2' relaxation of protonated and non-protonated carbon sites ($T_{2ar}'^{H}$ and $T_{2ar}'^{N}$, respectively). To test this assumption, we carried out the measurements on a known compound, trimethoxy benzene (TMOB), which indeed confirmed the validity of the method (see Figures S3 and Table S3 in SI).

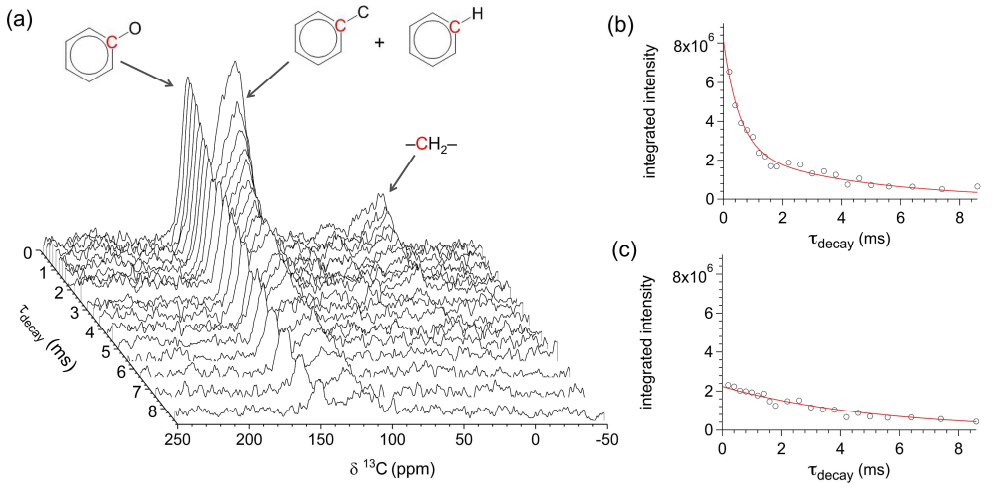

Figure 5. (a) ^{13}C DPMAS spectra of OMC300 obtained at 9.4 T with the spin-echo sequence for 0.2 ms ≤ τ ≤ 8.6 ms. (b) Integrated intensity of protonated and non-protonated aromatic carbons fitted to eq. (3). (c) Integrated intensity of phenolic aromatic carbons fitted to a single exponential function (eq. (4)).

Accordingly, the measurements of OMCs were carried out as follows. For each sample, we acquired a series of spin-echo DPMAS and CPMAS spectra as a function of τ, such as those shown for OMC300 in Figures 5a and S4a, respectively. The more sensitive CPMAS spectra were acquired with the sole purpose of obtaining accurate values T'^{H}_{2ar} and T'^{N}_{2ar} for protonated and non-protonated carbons resonating at 110 ppm ≤ δ_{13C} ≤140 ppm, as well as the relaxation time T'^{O}_{2ar} of phenolic carbons at $\delta_{13C} \cong$ 150 ppm. The T'^{H}_{2ar} and T'^{N}_{2ar} values were found by fitting the CPMAS data to the following equation:

$$M^{H+N}_{arCP}(\tau) = M^{H}_{arCP} e^{-2n\tau_R/T'^{H}_{2ar}} + M^{N}_{arCP} e^{-2n\tau_R/T'^{N}_{2ar}}, \quad (1)$$

where $M^{H+N}_{arCP}(\tau)$ is the intensity of the aromatic band after subtracting the deconvoluted peak representing the phenolic carbons, while M^{H}_{arCP} and M^{N}_{arCP} represent the transverse CPMAS magnetizations at $\tau = 2n\tau_R = 0$. Similarly, T'^{O}_{2ar} could be obtained by fitting the phenolic intensity $M^{O}_{arCP}(\tau)$ to a single exponential function,

$$M^{O}_{arCP}(\tau) = M^{O}_{arCP} e^{-2n\tau_R/T'^{O}_{2ar}}. \quad (2)$$

We then used these T'^{H}_{2ar}, T'^{N}_{2ar} and T'^{O}_{2ar} values to fit the less intense, but quantitative, DMPAS spectra to a pair of similar equations,

$$M^{H+N}_{arDP}(\tau) = M^{H}_{arDP} e^{-2n\tau_R / T'^{H}_{2ar}} + M^{N}_{arDP} e^{-2n\tau_R / T'^{N}_{2ar}} \quad (3)$$

and

$$M^{O}_{arDP}(\tau) = M^{O}_{arDP} e^{-2n\tau_R / T'^{O}_{2ar}}, \quad (4)$$

and thereby derive the accurate aromatic intensities M^{H}_{arDP}, M^{N}_{arDP} and M^{O}_{arDP} (Figure 5b,c). Finally, the quantitative values of f^{N}_{ar}, f^{H}_{ar} and f^{O}_{ar} fractions are given by

$$f^{X}_{ar} = \frac{M^{X}_{arDP}}{M^{H}_{arDP} + M^{N}_{arDP} + M^{O}_{arDP}}, \quad (5)$$

where *X* = *H*, *N*, and *O*. The results are summarized in Table 2, where the relative carbon intensities F^{X}_{ar} are referred to the overall carbon content, $F^{X}_{ar} = F_{ar} f^{X}_{ar}$.

Table 2. The distribution of carbon functionalities in OMC materials obtained from SSNMR analysis.

Sample	F_{ar} [a]	F_{al} [a]	F^{H}_{ar} [b]	F^{N}_{ar} [b]	F^{O}_{ar} [b]
OMC80	0.83 (2)[c]	0.17 (2)	-	-	-
OMC120	0.85 (2)	0.15 (2)	-	-	-
OMC300	0.91 (2)	0.09 (2)	0.48	0.24	0.19
OMC400	0.96 (1)	0.04 (1)	0.53	0.33	0.11
OMC500	0.97 (1)	0.03 (1)	0.53	0.38	0.06

[a] Relative fractions of aromatic and aliphatic carbons; [b] relative fractions of protonated, non-protonated and phenolic aromatic carbons in pyrolyzed samples, normalized such that $F^{H}_{ar} + F^{N}_{ar} + F^{O}_{ar} = F_{ar}$ (for each value, relative estimated error is ±5%); [c] the absolute error is given in parenthesis.

As a cross-check, for samples OMC300 and OMC500 the relative atomic concentrations of carbon and oxygen from Table 2 agree well with the results of elemental analysis given in Table 1. Given the inherent experimental uncertainties in both SSNMR and elemental analysis data, a good overall

agreement between the two sets of results gives us confidence about the viability of the proposed average structures. In one case, namely OMC400, the oxygen concentration obtained from elemental analysis (8.6 at.%) is considerably higher, in relative terms, than the NMR-derived result, as the F_{ar}^{O} value of 0.11 would translate to ~6.5 at.% of oxygen. Note, however, that the elemental analysis of oxygen relied on the difference between the total mass and the mass of carbon and hydrogen, which may have contributed to the larger error.

Structural Evolution of OMCs. Based on ^{13}C chemical shift information, quantitative recognition of carbon functionalities (Table 2) and the results of elemental analysis (Table 1), the chemical reactions that lead to their formation of OMCs as well as their average molecular structures can now be considered.

Chemical Evolution of Molecular Networks. Table 2 shows that pyrolysis results in the concomitant increase of F_{ar}^{H} and F_{ar}^{N}, as well as decrease of F_{ar}^{O}. These results are consistent with the growth of polycyclic aromatic clusters with higher average number of fused rings. To illustrate this point we note that in a linear molecule containing *n* fused aromatic rings, $f_{ar}^{N} = 0.20$ for *n* = 2, 0.29 for *n* = 3 and 0.33 for *n* = 4 (note that in such case F_{al} = 0 and thus $F_{ar}^{X} = f_{ar}^{X}$). Furthermore, the f_{ar}^{N} values strongly depend on the number of intermolecular links and additional substitutions. For example, if just one of the protonated carbons forms a link to another molecule, the f_{ar}^{N} values are elevated to 0.30 for *n* = 2, 0.36 for *n* = 3 and 0.39 for *n* = 4. A replacement of one of the hydrogen atoms with an OH group will not affect the f_{ar}^{N} values, but instead reduce f_{ar}^{H} by $f_{ar}^{O} = (4n+2)^{-1}$, etc. (see section S5 in SI).

Clearly, the data contained in Tables 1 and 2 should not be matched to a single molecular unit. Indeed, previous studies have amply demonstrated that pyrolysis of carbonaceous materials inevitably leads to a distribution of structural topologies, composed of various interconnected clusters of aromatic rings[37-39]. For example, Wornat et al. identified over 60 different species in their extensive analysis of volatile products of the pyrolysis of catechol[37], the majority of which were also observed in the

coal products[40]. The molecular evolution of OMCs is also complex, but some of the key chemical reactions leading to their formation can be deduced from our quantitative analyses.

OMC80 and OMC120. The ^{13}C spectra of $OMC80_{13C}$ and $OMC120_{13C}$ (Figure 2b) revealed that virtually all of the formaldehyde carbons were converted to methylene groups at temperature below 80 °C, forming either one or two $–CH_2–$ links between adjacent six-membered rings, as discussed earlier and shown in Figures 6 and 7, respectively. The presence of two links is proposed because (i) the observed F_{al} values are higher than expected for linear structures (Figure 6), (ii) the initial reaction involved 1 : 1.6 molar mixture of resorcinol and formaldehyde (we should note, however, that some undetermined amount of formaldehyde was likely lost during the reaction due to evaporation), and (iii) their presence is consistent with the chemical shifts observed in the spectra of $OMC80_{13C}$ and $OMC120_{13C}$ (*vide supra*).

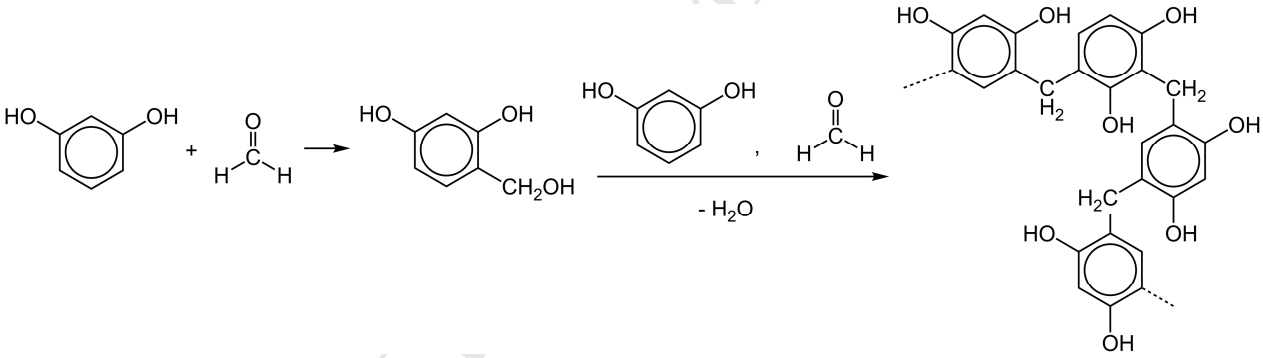

Figure 6. Polymerization reaction below 80 ˚C.

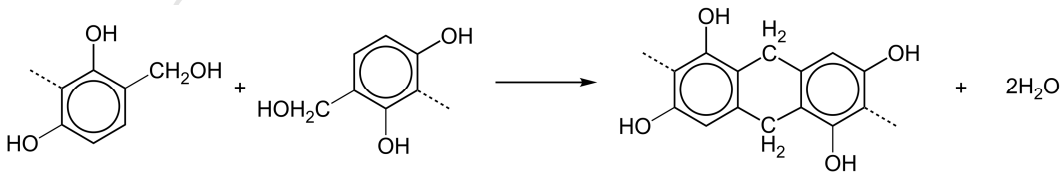

Figure 7. Formation of two methylene bonds at 80 ˚C and 120 ˚C[20].

OMC300. The ^{13}C spectra of OMC300 and $OMC300_{13C}$ showed that the structural changes upon pyrolysis at 300 ˚C include increased carbon aromaticity (see Table 2), the onset of incorporation of ^{13}C-labeled atoms into the aromatic structures, and the appearance of methyl groups. In view of these findings, we conclude that the aromatic ring condensation reactions initiate below 300 °C, most likely leading to the formation of three-membered aromatic clusters according to Figure 8:

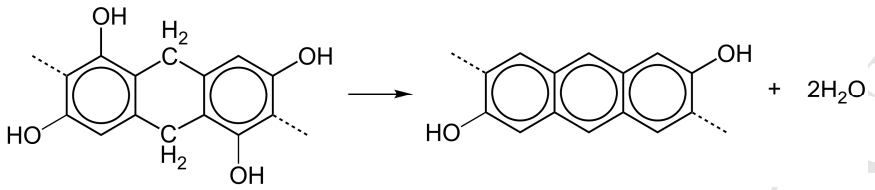

Figure 8. Formation of three membered aromatic cluster.

The formation of methyl groups most likely involves radical species, as proposed in Figure 9:

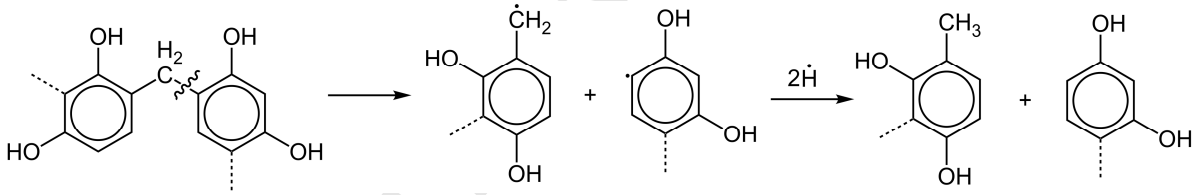

Figure 9. Formation of methyl groups at 300 ˚C[20].

Note that the presence of free radicals in OMC300, OMC400 and OMC500 was confirmed by the EPR spectroscopy (Figure S6 in SI). The high F_{ar}^{O} value in OMC300 is mainly due to carbons associated with the hydroxyl groups, although initiation of the reactions presented in Figure 10 below, such as the formation of phenol ether links, Ph–O–Ph, cannot be excluded.

OMC400 and OMC500. The elemental analysis data show a reduction in relative O and H contents in OMC400 and OMC500 with respect to OMC300. The concurrent changes in carbon speciation between 300 °C and 500 °C are as follows: F_{ar}^{O} diminishes from 0.19 to 0.06, F_{ar}^{N} increases from 0.24

to 0.38, whereas F_{ar}^{H} increases slightly from 0.48 to 0.53 (in fact the value of f_{ar}^{H} is almost unchanged). To account for these changes, we postulate a series of reactions shown in Figure 10:

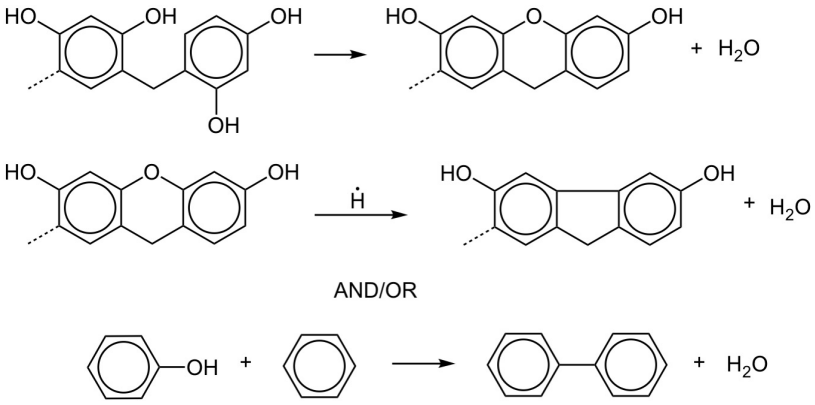

Figure 10. Formation of phenyl ether links, 5-membered rings and biphenyl species in OMC formed at pyrolysis temperatures above 300 ˚C[20].

Note that these reactions are consistent with the observed chemical shifts, and that the last two involve radical intermediates. Finally, in the spectra of OMC400 and OMC500 the relative aliphatic intensity become further reduced, to 4% and 3%, respectively, which is accompanied by increased incorporation of ^{13}C-carbons into aromatic rings in $OMC400_{13C}$ and $OMC500_{13C}$. All these changes are consistent with the advancing polycyclization and the resulting increase of the average size of aromatic clusters. In addition to reactions proposed in Figures 8 and 10, polycyclization may proceed via the reactions similar to those shown in Figure 11:

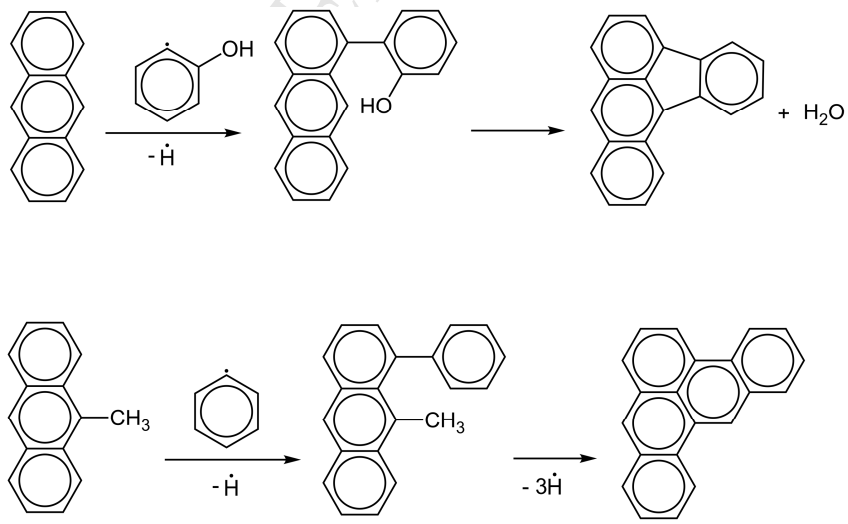

Figure 11. Polycyclization of OMCs during pyrolysis at 400 ˚C and 500 ˚C.

Average Molecular Structures of OMCs. The structural frameworks of OMC300, OMC400 and OMC500 materials resulting from pyrolysis of the resorcinol-formaldehyde polymer are expected to be composed of a variety of interlinked species described above. Based on the distribution of carbon functionalities in Table 2, the *average* sizes of aromatic clusters in OMC300, OMC400 and OMC500 are close to 2, 3 and 4 respectively, however, each sample undoubtedly contains a wide distribution of molecular units. For example, based on Figures 6 through 9, it appears unlikely that OMC300 contains any 2-ring structures, and instead is primarily composed of interconnected single-ring and triple-ring structures. Figure 12 shows the representation of an average structure proposed for OMC500, constructed such that it is consistent with the spectroscopic results, elemental analysis data and the chemical transformations described above in this study.

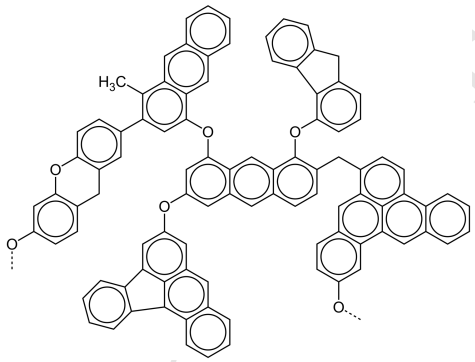

Figure 12. Representation of average extended molecular network of OMC500 consistent with the ^{13}C chemical shift information, elemental analysis (Table 1) and quantitative measurements of carbon functionalities by SSNMR (Table 2).

We finally note that pyrolysis at temperatures above 500 °C results in further polycyclization. Although we could not elicit NMR signals from the OMC900 material, the results of elemental analysis

indicate that it must be composed of large aromatic clusters containing on average >200 aromatic rings. The polycyclization results in the contraction of the OMCs' molecular structure, which is reflected by the reductions of the unit cell size, pore width and wall thickness, and the corresponding increases of surface areas and total pore volumes (Table 1).

4. CONCLUSION

SSNMR techniques were combined with elemental analysis and textural characterization to ascertain the atomic-scale structures of OMC materials prepared using Pluronic F127 as template with resorcinol and formaldehyde as polymerizing precursors. Analysis of ^{13}C DPMAS and CPMAS spectra of natural abundance and isotope enriched samples provided quantitative distribution of carbon functionalities at various stages of pyrolysis and offered valuable insights into the pyrolysis mechanisms. Some of the important findings are as follows: (1) the formaldehyde carbons were fully converted to $–CH_2–$ links between adjacent six-membered rings at temperature below 80 °C, (2) the structural changes upon pyrolysis include the formation of methyl groups (below 300 °C), gradual incorporation of aliphatic carbons into aromatic structures (advanced at temperatures above 300 °C), and the formation of polycyclic aromatic substructures via a series of deoxygenation and radical reactions, and (3) the average sizes of aromatic clusters in OMC300, OMC400, and OMC500 are close to 2, 3 and 4 respectively, whereas OMC900 comprises a highly carbonized aromatic network composed of much larger clusters. As we have noted throughout this study, each of the studied materials contains a distribution of molecular units. Likewise, the pyrolysis routes proposed here, while consistent with the experimental data and differing from some of the earlier studies, are undoubtedly simplified. To further refine the understanding of the underlying reaction mechanisms, the proposed methodology can be combined with TGA and GC-MS, and applied to an expanded set of temperature values.

Electronic supplemental information: Physical characterization data, including N_2 sorption isotherms, pore size distributions, powder XRD patterns; $^{13}C\{^1H\}$ SSNMR spectra; and EPR spectra.

Acknowledgment

This research is supported by the U.S. Department of Energy, Office of Basic Energy Sciences, Division of Chemical Sciences, Geosciences, and Biosciences through the Ames Laboratory. The Ames Laboratory is operated for the U.S. Department of Energy by Iowa State University under Contract No. DE-AC02-07CH11358.

References:

[1] H. Tamon, H. Ishizaka, T. Araki, M. Okazaki, Control of mesoporous structure of organic and carbon aerogels, Carbon 36 (1998) 1257-1262.
[2] R. Ryoo, S.H. Joo, S. Jun, Synthesis of highly ordered carbon molecular sieves via template-mediated structural transformation, J. Phys. Chem. B 103 (1999) 7743-7746.
[3] A.G. Kong, Y.Y. Kong, X.F. Zhu, Z. Han, Y.K. Shan, Ordered mesoporous Fe (or Co)-N-graphitic carbons as excellent non-precious-metal electrocatalysts for oxygen reduction, Carbon 78 (2014) 49-59.
[4] A.H. Lu, A. Kiefer, W. Schmidt, F. Schuth, Synthesis of polyacrylonitrile-based ordered mesoporous carbon with tunable pore structures, Chem. Mater. 16 (2004) 100-103.
[5] C.D. Liang, S. Dai, Synthesis of mesoporous carbon materials via enhanced hydrogen-bonding interaction, J. Am. Chem. Soc. 128 (2006) 5316-5317.
[6] C.D. Liang, K.L. Hong, G.A. Guiochon, J.W. Mays, S. Dai, Synthesis of a large-scale highly ordered porous carbon film by self-assembly of block copolymers, Angew. Chem. Int. Ed. 43 (2004) 5785-5789.
[7] T.W. Kim, P.W. Chung, Slowing, II, M. Tsunoda, E.S. Yeung, V.S.Y. Lin, Structurally ordered mesoporous carbon nanoparticles as transmembrane delivery vehicle in human cancer cells, Nano Lett. 8 (2008) 3724-3727.
[8] Y. Fang, D. Gu, Y. Zou, Z.X. Wu, F.Y. Li, R.C. Che, Y.H. Deng, B. Tu, D.Y. Zhao, A low-concentration hydrothermal synthesis of biocompatible ordered mesoporous carbon nanospheres with tunable and uniform size, Angew. Chem. Int. Ed. 49 (2010) 7987-7991.
[9] Y.Y. Lv, Z.X. Wu, Y. Fang, X.F. Qian, A.M. Asiri, B. Tu, D.Y. Zhao, Hierarchical mesoporous/microporous carbon with graphitized frameworks for high-performance lithium-ion batteries, APL Mater. 2 (2014) 113302.
[10] L.C. Jia, G.P. Mane, C. Anand, D.S. Dhawale, Q.M. Ji, K. Ariga, A. Vinu, A facile photo-induced synthesis of cooh functionalized meso-macroporous carbon films and their excellent sensing capability for aromatic amines, Chem. Commun. 48 (2012) 9029-9031.
[11] S.M. Mahurin, J.S. Lee, X. Wang, S. Dai, Ammonia-activated mesoporous carbon membranes for gas separations, J. Membr. Sci. 368 (2011) 41-47.

[12] S.H. Joo, S.J. Choi, I. Oh, J. Kwak, Z. Liu, O. Terasaki, R. Ryoo, Ordered nanoporous arrays of carbon supporting high dispersions of platinum nanoparticles, Nature 412 (2001) 169-172.
[13] S.H. Joo, S. Jun, R. Ryoo, Synthesis of ordered mesoporous carbon molecular sieves CMK-1, Microporous Mesoporous Mater. 44 (2001) 153-158.
[14] Y. Meng, D. Gu, F.Q. Zhang, Y.F. Shi, H.F. Yang, Z. Li, C.Z. Yu, B. Tu, D.Y. Zhao, Ordered mesoporous polymers and homologous carbon frameworks: Amphiphilic surfactant templating and direct transformation, Angew. Chem. Int. Ed. 44 (2005) 7053-7059.
[15] Y. Meng, D. Gu, F.Q. Zhang, Y.F. Shi, L. Cheng, D. Feng, Z.X. Wu, Z.X. Chen, Y. Wan, A. Stein, D.Y. Zhao, A family of highly ordered mesoporous polymer resin and carbon structures from organic-organic self-assembly, Chem. Mater. 18 (2006) 4447-4464.
[16] J. Gorka, A. Zawislak, J. Choma, M. Jaroniec, Koh activation of mesoporous carbons obtained by soft-templating, Carbon 46 (2008) 1159-1161.
[17] F.Q. Zhang, Y. Meng, D. Gu, Y. Yan, Z.X. Chen, B. Tu, D.Y. Zhao, An aqueous cooperative assembly route to synthesize ordered mesoporous carbons with controlled structures and morphology, Chem. Mater. 18 (2006) 5279-5288.
[18] X.Q. Wang, C.D. Liang, S. Dai, Facile synthesis of ordered mesoporous carbons with high thermal stability by self-assembly of resorcinol-formaldehyde and block copolymers under highly acidic conditions, Langmuir 24 (2008) 7500-7505.
[19] Y.J. Kim, M.I.I. Kim, C.H. Yun, J.Y. Chang, C.R. Park, M. Inagaki, Comparative study of carbon dioxide and nitrogen atmospheric effects on the chemical structure changes during pyrolysis of phenol-formaldehyde spheres, J. Colloid Interface Sci. 274 (2004) 555-562.
[20] H.Y. Jiang, J.G. Wang, S.Q. Wu, Z.Q. Yuan, Z.L. Hu, R.M. Wu, Q.L. Liu, The pyrolysis mechanism of phenol formaldehyde resin, Polym. Degrad. Stab. 97 (2012) 1527-1533.
[21] K.M. Mao, G.J. Kennedy, S.M. Althaus, M. Pruski, Determination of the average aromatic cluster size of fossil fuels by solid-state NMR at high magnetic field, Energy Fuels 27 (2013) 760-763.
[22] M.S. Solum, R.J. Pugmire, D.M. Grant, C-13 solid-state NMR of argonne premium coals, Energy Fuels 3 (1989) 187-193.
[23] S. Brunauer, P.H. Emmett, E. Teller, Adsorption of gases in multimolecular layers, J. Am. Chem. Soc. 60 (1938) 309-319.
[24] E.P. Barrett, L.G. Joyner, P.P. Halenda, The determination of pore volume and area distributions in porous substances .1. Computations from nitrogen isotherms, J. Am. Chem. Soc. 73 (1951) 373-380.
[25] Y. Huang, H.Q. Cai, T. Yu, F.Q. Zhang, F. Zhang, Y. Meng, D. Gu, Y. Wan, X.L. Sun, B. Tu, D.Y. Zhao, Formation of mesoporous carbon with a face-centered-cubic Fd(3)over-barm structure and bimodal architectural pores from the reverse amphiphilic triblock copolymer PPO-PEO-PPO, Angew. Chem. Int. Ed. 46 (2007) 1089-1093.
[26] M. Schoeffel, N. Brodie-Linder, F. Audonnet, C. Alba-Simionesco, Wall thickness determination of hydrophobically functionalized MCM-41 materials, J. Mater. Chem. 22 (2012) 557-567.
[27] C.E. Snape, D.E. Axelson, R.E. Botto, J.J. Delpuech, P. Tekely, B.C. Gerstein, M. Pruski, G.E. Maciel, M.A. Wilson, Quantitative reliability of aromaticity and related measurements on coals by C-13 NMR - a debate, Fuel 68 (1989) 547-560.
[28] O.H. Han, Y.K. Bae, Solid-state NMR study on the structure and dynamics of triblock copolymer P123 remaining in SBA-15 after solvent washing, Bull. Korean Chem. Soc. 29 (2008) 911-912.
[29] J. Ma, C. Guo, Y. Tang, J. Wang, L. Zheng, X. Liang, S. Chen, H. Liu, Microenvironmental and conformational structure of triblock copolymers in aqueous solution by H-1 an C-13 NMR spectroscopy, J. Colloid Interface Sci. 299 (2006) 953-961.
[30] D.D. Werstler, Quantitative C-13 NMR characterization of aqueous formaldehyde resins .2. Resorcinol-formaldehyde resins, Polymer 27 (1986) 757-764.
[31] The chemical shifts were estimated by ACD Labs Software v11.01, via Scifinder; chemical abstracts service. https://scifinder.cas.org/scifinder/view/scifinder/scifinderExplore.jsf.

[32] Spectral database for organic compounds, sdbs. http://sdbs.db.aist.go.jp/sdbs/cgi-bin/cre_index.cgi.
[33] J. Grobelny, J. Obrzut, F.E. Karasz, Solid-state C-13 NMR-study of neutral insulating and electrochemically doped conducting poly(para-phenylene vinylene), Synth. Met. 29 (1989) E97-E102.
[34] J.C.C. Freitas, F.G. Emmerich, G.R.C. Cernicchiaro, L.C. Sampaio, T.J. Bonagamba, Magnetic susceptibility effects on C-13 MAS NMR spectra of carbon materials and graphite, Solid State Nucl. Magn. Reson. 20 (2001) 61-73.
[35] S.J. Opella, M.H. Frey, Selection of non-protonated carbon resonances in solid-state nuclear magnetic-resonance, J. Am. Chem. Soc. 101 (1979) 5854-5856.
[36] K.M. Mao, G.J. Kennedy, S.M. Althaus, M. Pruski, Spectral editing in C-13 solid-state NMR at high magnetic field using fast MAS and spin-echo dephasing, Solid State Nucl. Magn. Reson. 47-48 (2012) 19-22.
[37] M.J. Wornat, E.B. Ledesma, N.D. Marsh, Polycyclic aromatic hydrocarbons from the pyrolysis of catechol(ortho-dihydroxybenzene), a model fuel representative of entities in tobacco, coal, and lignin, Fuel 80 (2001) 1711-1726.
[38] S.E. Stein, Thermal-reactions and properties of polycyclic aromatic-hydrocarbons, Acc. Chem. Res. 24 (1991) 350-356.
[39] E. Fitzer, Thermal-degradation of polymers to polymeric carbon - an approach to the synthesis of new materials, Angew. Chem. Int. Ed. 19 (1980) 375-385.
[40] E.B. Ledesma, M.A. Kalish, P.F. Nelson, M.J. Wornat, J.C. Mackie, Formation and fate of PAH during the pyrolysis and fuel-rich combustion of coal primary tar, Fuel 79 (2000) 1801-1814.

ACCEPTED MANUSCRIPT

ACCEPTED MANUSCRIPT

Supporting Information for

Quantitative Atomic-Scale Structure Characterization of Ordered Mesoporous Carbon Materials by Solid State NMR

Zhuoran Wang, Naftali Opembe, Takeshi Kobayashi, Nicholas C. Nelson, Igor I. Slowing and Marek Pruski**

Department of Chemistry and U.S. Department of Energy Ames Laboratory, Iowa State University, Ames, Iowa 50011, United States

S1. Physical characterizations of OMC materials

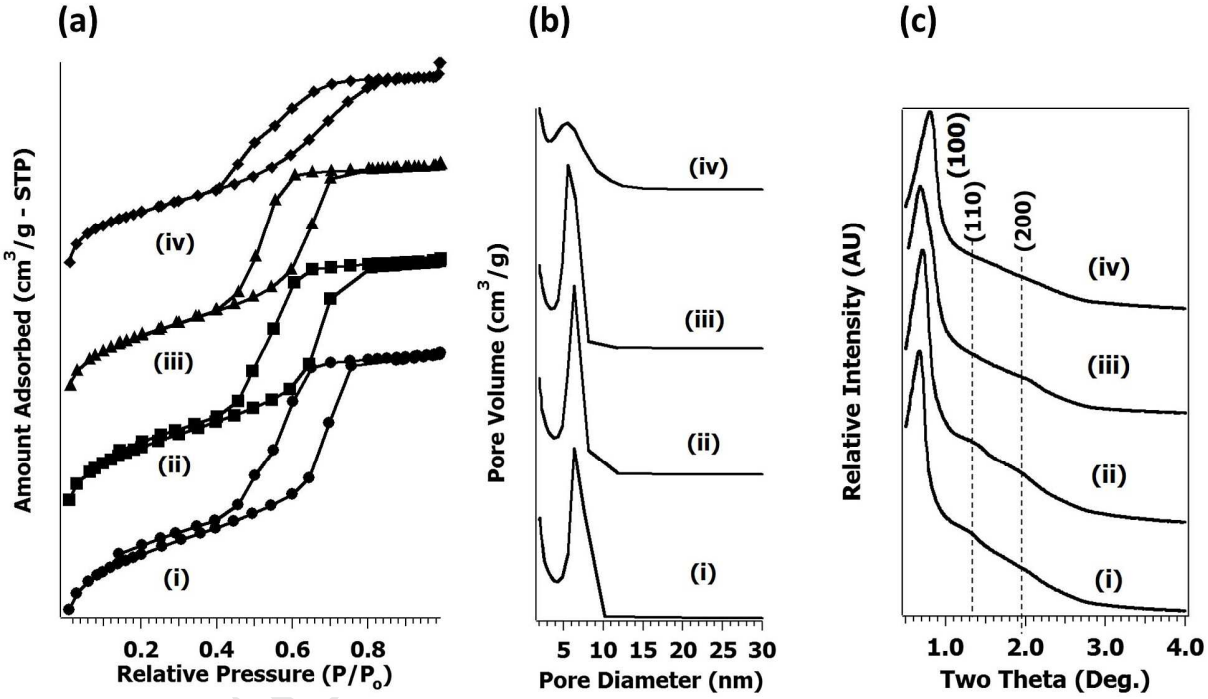

Figure S1. N_2 sorption isotherms (a), pore size distributions (b), and powder XRD patterns (c) for OMC300 (i), OMC400 (ii), OMC500 (iii), and OMC900 (iv).

S2. $^{13}C\{^1H\}$ CPMAS experiments

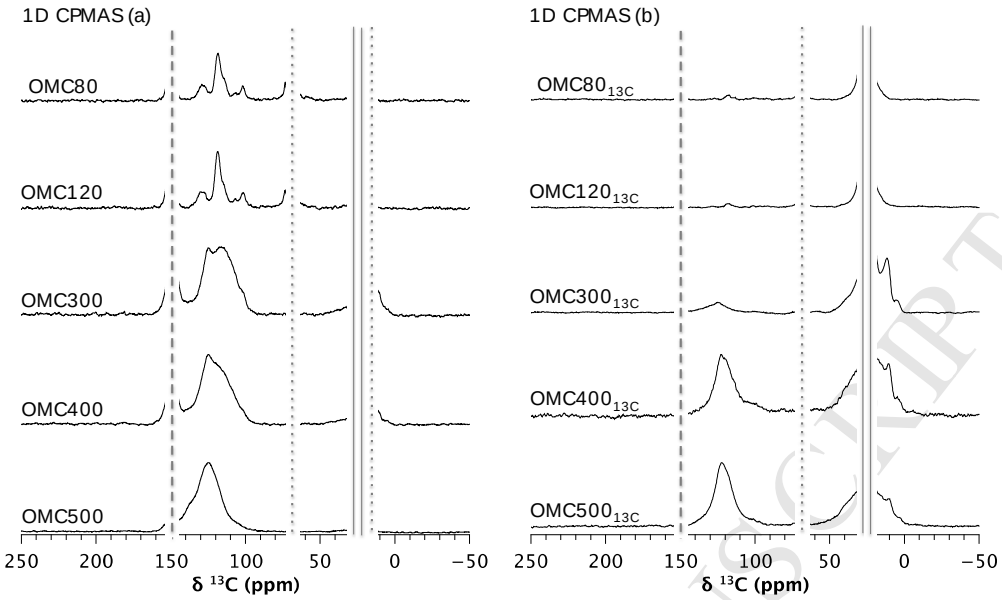

Figure S2. The $^{13}C\{^1H\}$ CPMAS spectra of natural abundance (a) and isotope enriched (b) OMC materials. The spectra were acquired at 14.1 T using ν_R = 40 kHz, $\nu_{RF}(^1H)$ = 60 kHz during CP, $\nu_{RF}(^{13}C)$ = 100 kHz during CP, τ_{CP} = 1.5 ms, $\nu_{RF}(^1H)$ = 10 kHz during TPPM decoupling, τ_{RD} = 1 s, NS = 8000 (a) and NS = 3600 (b).

S3. Dipolar dephasing experiment for trimethoxy benzene (TMOB)

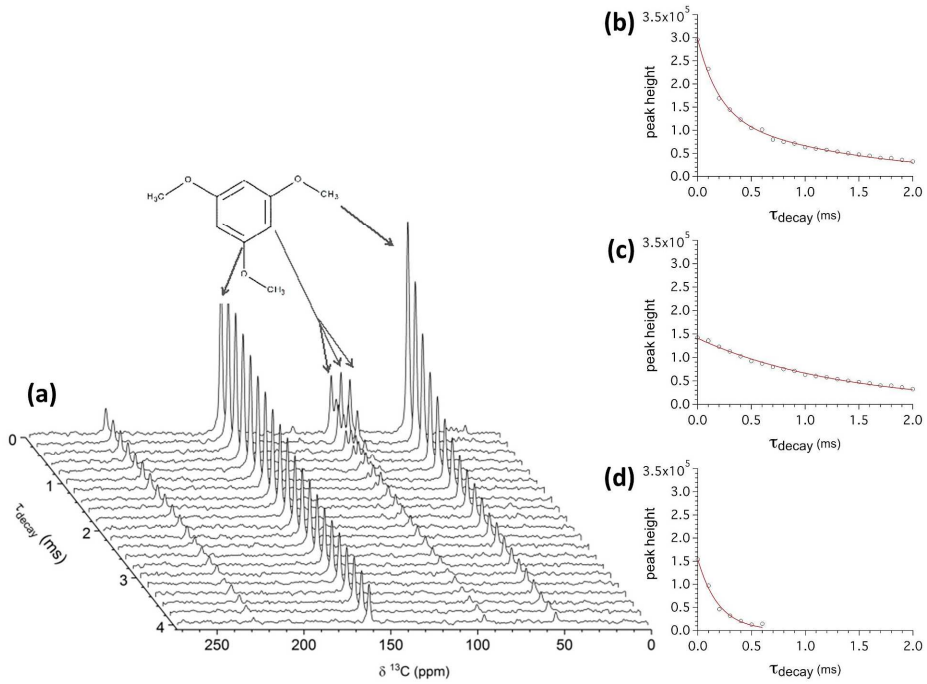

Figure S3. The ^{13}C CPMAS-based spin-echo 'dipolar dephasing' spectra of TMOB obtained at 9.4 T with different decay times (a) and the fitting curves for aromatic carbons (b-d). (b) double exponential fitting to the total peak height of all aromatic carbons; (c) single exponential fitting to the peak height of non-protonated aromatic carbons; (d) single exponential fitting to the peak height of protonated aromatic carbons.

Table S3. The T_2' values and intensity ratios extracted from curve fittings in Figure S3.

Methods	Double Exponential	Single Exponential
$T_{2ar}'^{H}$ (ms)	0.19	0.19
$T_{2ar}'^{O}$ (ms)	1.34	1.33
$M_{ar}^{H} : M_{ar}^{O}$	1.60 : 1.38	1.54 : 1.41

S4. Quantification of carbon functionalities in OMCs.

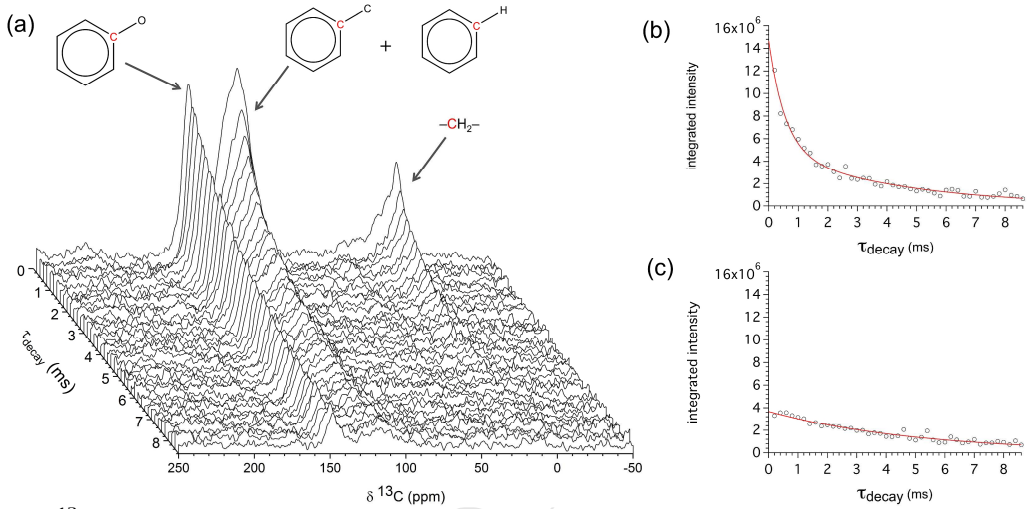

Figure S4. (a) ^{13}C CPMAS-based spin-echo 'dipolar dephasing' spectra of OMC300 obtained at 9.4 T with delays 0.2 ms ≤ τ ≤ 8.6 ms. (b) Integrated intensity of protonated and non-protonated aromatic carbons fitted to eq. (1). (c) Integrated intensity of phenolic aromatic carbons fitted to a single exponential function (eq. (2)).

Table S4. The summary of T_2' values and intensity ratios between different carbon species for OMC300, OMC400 and OMC500 obtained from SSNMR analysis.

Sample	OMC300	OMC400	OMC500
$T_{2ar}'^{H}$ (ms)	0.6	0.6	1.0
$T_{2ar}'^{N}$ (ms)	4.3	4.4	7.0
$T_{2ar}'^{O}$ (ms)	5.1	5.9	8.0
$M_{arDP}^{H} : M_{arDP}^{N} : M_{arDP}^{O}$	1 : 0.48 : 0.40	1 : 0.62 : 0.19	1 : 0.71 : 0.10

S5. Fractions of non-protonated carbons in fused aromatic rings.

Let's consider a linear molecule comprised of *n* aromatic rings, as shown below:

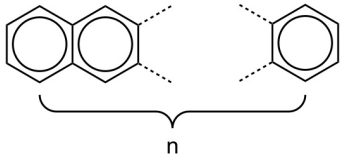

It is easy to show that for such a molecule

$$f_{ar}^{N} = \frac{n-1}{2n+1}, \qquad \text{(s1)}$$

which yields $f_{ar}^{N} = 0.20$ for n = 2, 0.29 for n = 3 and 0.33 for n = 4 (note that F_{al} = 0 and thus $F_{ar}^{X} = f_{ar}^{X}$). It is important to note that the f_{ar}^{N} values strongly depend on the number of intermolecular links and additional substitutions. For example, if just one of the protonated carbons forms a link to another molecule, eq. (s1) becomes

$$f_{ar}^{N} = \frac{2n-1}{4n+2}, \qquad \text{(s2)}$$

which elevates the f_{ar}^{N} values to 0.30 for n = 2, 0.36 for n = 3 and 0.39 for n = 4. A replacement of one of the hydrogen atoms with an OH group will not affect the f_{ar}^{N} values, but instead reduce f_{ar}^{H} by $f_{ar}^{O} = (4n+2)^{-1}$, etc.

S6. Continuous Wave Electron Paramagnetic Resonance (cwEPR). With the concern that radicals may be present in OMC materials due to the thermal treatment, The cwEPR spectra were taken of OMC300, OMC400, and OMC500. In order to obtain trustable spectrum, for each sample, two EPR tubes were prepared with the same amount of sample. And, when taking the spectrum, tube was carefully placed in the same position of the resonator cavity.

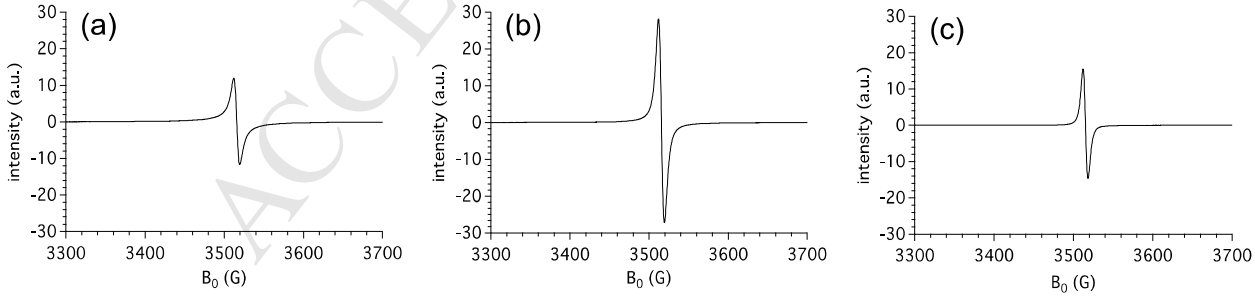

Figure S6. The CW X-band room temperature EPR spectra of OMC300 (a), OMC400 (b) and OMC500 (c). All three spectra were taken using the same parameters: microwave frequency is 9.87GHz, power is 6.286mW, sweeping width is 500.0G, center field is 3500.00G. The spectrometer is Bruker ELEXYS E580 FT-EPR with ER 4122 SHQE resonator.

ACCEPTED MANUSCRIPT

S7. ^{13}C Chemical Shift Information for Polymerizing Precursors. For resorcinol, the ^{13}C chemical shifts are as follows: C1(C3) - 158 ppm; C2 - 104 ppm; C4(C6) - 108 ppm; and C5 - 132 ppm[1]. The ^{13}C chemical shift for formaldehyde is 195 ppm[2].

Reference:

[1] Spectral database for organic compounds, sdbs. http://sdbs.db.aist.go.jp/sdbs/cgi-bin/cre_index.cgi.
[2] S. Patchkovskii, J. Autschbach, T. Ziegler, Curing difficult cases in magnetic properties prediction with self-interaction corrected density functional theory, J. Chem. Phys. 115 (2001) 26-42.

ACCEPTED MANUSCRIPT